CATALYSIS

Nature of metal-support interaction for metal catalysts on oxide supports

Tairan Wang[1]†‡, Jianyu Hu[2]†, Runhai Ouyang[3]†, Yutao Wang[1], Yi Huang[4], Sulei Hu[2], Wei-Xue Li[1,5]*

The metal-support interaction is one of the most important pillars in heterogeneous catalysis, but developing a fundamental theory has been challenging because of the intricate interfaces. Based on experimental data, interpretable machine learning, theoretical derivation, and first-principles simulations, we established a general theory of metal-oxide interactions grounded in metal-metal and metal-oxygen interactions. The theory applies to metal nanoparticles and atoms on oxide supports and oxide films on metal supports. We found that for late-transition metal catalysts, metal-metal interactions dominated the oxide support effects and suboxide encapsulation over metal nanoparticles. A principle of strong metal-metal interactions for encapsulation occurrence is formulated and substantiated by extensive experiments including 10 metals and 16 oxides. The valuable insights revealed on (strong) metal-support interaction advance the interfacial design of supported metal catalysts.

Oxide-supported transition metal (TM) catalysts are essential for petrochemical refining and industrial chemical manufacturing, as well as for environmental control systems such as exhaust catalysts (*1*). How metals interact with gaseous reactants and support underneath, i.e., metal-reactant interactions (MRIs) and metal-support interactions (MSIs), are two cornerstones of supported metal catalysts (*2*, *3*). Whereas MRI determines activity and selectivity (*4*), MSI helps to stabilize dispersed catalysts (*5*, *6*) and affects interfacial processes such as charge transfer, chemical composition, perimeter sites, particle morphology, and suboxide encapsulation (*7*, *8*). Modulation of MSIs is thus one of the few strategies for enhancing the catalyst performance (*9*).

Despite the critical role of MSIs in many catalytic properties (*10*), including sintering resistance (*11*), MSIs can be difficult to characterize because they are sensitive to the composition of metals and supports (*12*, *13*) and change substantially with corresponding size and morphology, preparations and reaction conditions, among other things (*14*). These complexities substantially limit the investigation of structure-function relations. For example, strong MSIs (SMSIs), which were originally used to describe the encapsulation of supported metal nanoparticles (NPs) by suboxide layers at elevated temperatures (*15*), have received much attention recently and have been thought of as the origin of many prominent interfacial processes (*16*). However, fundamental questions remain about the nature of MSIs and SMSIs and their influence on interfacial processes in general and encapsulation in particular (*17*).

To quantify MSIs, numerous descriptors have been proposed through experimental and symbolic regression approaches (*18*, *19*) such as metal oxophilicity (*20*), metal surface energy (*21*), and electron density (*22*). Moreover, the presence of metal-metal bonding in metal-oxide interfaces has also been observed (*15*, *18*, *23*, *24*). However, developing a comprehensive theory of MSIs for metal catalysts on oxide supports remains a major challenge in heterogeneous catalysis. Here, we used experimental data, interpretable machine learning (*25*, *26*), theoretical derivation, and first-principles simulations to establish a general theory of MSIs grounded in metal-metal interactions (MMIs) and metal-oxygen interactions (MOIs). Specifically, advanced symbolic regression (*27*) was used on 178 experimentally determined interfacial adhesion energies between metal NPs and oxide supports from the literature, leading to the discovery of a predictive formula for MSIs. This formula is derivable under the nearest-neighbor approximation and is generalizable to other interfacial systems of oxide-supported metal atoms and metal-supported oxide films, as demonstrated by density functional theory (DFT) calculations.

We found that for supported late TM catalysts, the differences in MMIs determine the support effects that distinguish the MSI strengths from different oxides, although the MOI becomes dominant to the MSI when considering other metals. Molecular dynamics (MD) simulations using global neural network potentials (*28*) revealed that strong MMI not only promotes the formation of metal-metal bonds across the encapsulation interface, but also controls the encapsulation kinetics. Thus, we formulated a principle that strong MMIs, rather than strong oxophilic MSIs, determine whether encapsulation occurs, which is substantiated by extensive experiments including 10 late TMs and 16 oxides. The theory provides a comprehensive framework for understanding MSIs and SMSIs and various interfacial processes, which will advance the precise design of metal catalysts on supports.

Formula of MSIs

We used the sure independence screening and sparsifying operator (SISSO) (*27*) to determine the functional form of MSIs (Fig. 1A). Specifically, the adhesion energy E_{adh} between metal nanoparticles and oxide supports, a critical variable for quantifying MSIs, was compiled from reported experimental values that encompassed 178 metal-oxide interfaces across 25 metals and 27 oxides (Fig. 1B and table S1). To ensure data reliability, the collected data were obtained from the consistent sessile-drop method for liquid metal particles on oxides in wetting experiments, and the influence of the surface cleanness was reported and discussed previously (*20*).

To find the physical MSI model, we leverage symbolic regression by considering all possible physical quantities relevant to the metal-oxide interface as primary features (50 in total and listed in table S2). Many of them were proposed as descriptors of MSIs (*18*–*22*). After removing redundant ones through backward elimination and cross-validation, 14 highly independent and important features were retained, and their correlations are presented as Pearson similarities (Fig. 1C). A comprehensive exploration of >30 billion mathematical expressions was conducted by integrating these distilled features using simple mathematic operators to ensure model interpretability without compromising accuracy. Through compressed sensing, an optimal two-dimensional model was identified. Further increasing the complexity would enhance training accuracy, but at the cost of interpretability and generalizability, as detailed in the supplementary materials.

The developed model exhibited excellent performance on the test dataset with a root mean square error of 14 meV/Å^2 (fig. S1), which is comparable to experimental uncertainty (ranging from 6 to 19 meV/Å^2) (*29*) and outperforms neural network models (fig. S2) and previous descriptors (table S4). The obtained MSI model is composed of the MOI and MMI terms:

$$E_{adh} = \beta_1 \bullet Q(MO) + \beta_2 \bullet Q(MM') + \beta_0 \quad (1)$$

with

[1]Key Laboratory of Precision and Intelligent Chemistry, School of Chemistry and Materials Science, iChEM, University of Science and Technology of China, Hefei, China. [2]Hefei National Research Center for Physical Sciences at the Microscale, University of Science and Technology of China, Hefei, China. [3]Materials Genome Institute, Shanghai University, Shanghai, China. [4]School of Emerging Technology, University of Science and Technology of China, Hefei, Anhui, China. [5]Hefei National Laboratory, University of Science and Technology of China, Hefei, Anhui, China.
*Corresponding author. Email: wxli70@ustc.edu.cn
†These authors contributed equally to this work.
‡Present address: Tairan Wang Clean Energy Research Platform, King Abdullah University of Science and Technology (KAUST), Thuwal, Kingdom of Saudi Arabia.

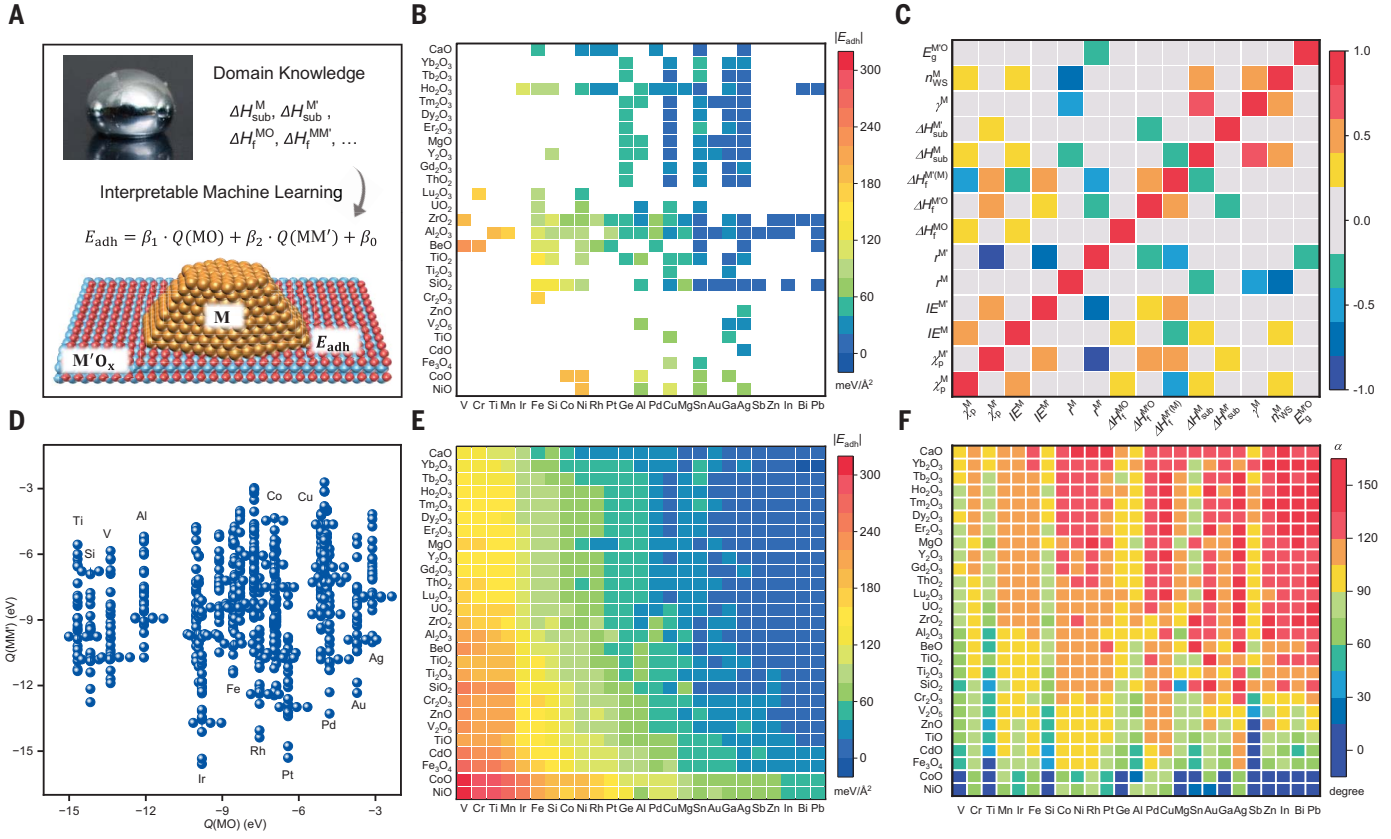

Fig. 1. Formulation of the MSI model. (**A**) A derivable formula was identified through interpretable machine learning. (**B**) Collected experimental adhesion energies $|E_{adh}|$ of metal-support systems from the literature (metals are shown on the *x* axis and supports on the *y* axis). (**C**) Pearson correlations between the selected 14 primary features. M denotes the element of supported metal and M′ refers to the metal in oxide. These features include Pauling electronegativity (χ_p), first ionization energy (IE), metallic radius of supported metal M (r^M), Shannon ionic radius of metal M′ ($r^{M'}$), formation enthalpy of most stable oxide of M (ΔH_f^{MO}), formation enthalpy of oxide ($\Delta H_f^{M'O}$), formation enthalpy of mixing at infinite dilution of unit M′ in M ($\Delta H_f^{MM'}$), sublimation enthalpy (ΔH_{sub}), surface energy of M (γ^M), electron density at the boundary of the Wigner-Seitz cell (n_{WS}), and bandgap energy of oxide ($E_g^{M'O}$). (**D**) The descriptors *Q*(MO) and *Q*(MM′), representing the oxophilicity and M′ affinity of M, respectively, for the considered systems. (**E**) Recovered image of (B) by filling out the white spots with $|E_{adh}|$ predicted by Eq. 1. (**F**) Predicted contact angles α of all the 675 metal-oxide interfaces.

$$Q(MO) = \Delta H_f^{MO} - \Delta H_{sub}^{M},$$
$$Q(MM') = \Delta H_f^{MM'} - \Delta H_{sub}^{M} - \Delta H_{sub}^{M'} \quad (2)$$

where M denotes the element of supported metal, M′ refers to the metal in oxide, ΔH_f^{MO} is the formation enthalpy of supported metal forming its most stable oxide, ΔH_{sub} is the sublimation enthalpy, and $\Delta H_f^{MM'}$ is the formation enthalpy of mixing M′ into M at infinite dilution and calculated based on Miedema's model (*30*) (see the supplementary materials), where β_0 = 16 meV/Å², $\beta_1 = c_1 \cdot \gamma^M \cdot \chi_p^{M'}/\chi_p^M$, and c_1 = 9.85 × 10^{-2}/eV. The ratio of Pauling electronegativity $\chi_p^{M'}/\chi_p^M$ shows the competitive bonding affinity of the two metal elements with oxygen, and systems with higher ratios are prone to having more interfacial M–O bonds. The surface energy of metal NPs, γ^M, is associated with van der Waals interfacial interactions, evident for weak MSIs (*21*), as depicted in fig. S3, where $\beta_2 = c_2 \cdot IE^M/\Delta H_f^{M'O}$, c_2 = −3.06 × 10^{-3}/Å². The magnitude of β_2 is high when M tends to bond with M′ because of its high first ionization energy IE^M and when M′ has weak bonding with oxygen or is in a low valence state with a low formation enthalpy of oxide support $|\Delta H_f^{M'O}|$.

Q(MO) in Eq. 2 is the oxophilicity per mole of M, which reflects the oxygen affinity of the supported metal M, as previously introduced by Campbell and co-workers (*20*, *29*), who discovered its linear correlation with adhesion energies. *Q*(MM′) is the formation enthalpy of the alloy per mole M and M′ from gaseous metal atoms, which reflects corresponding M′ affinity of M (see the supplementary materials). For example, the M′ affinity for Pd/TiO_2 means the Ti affinity of Pd. Compared with $\Delta H_f^{MO}$and ΔH_f^{MM}, *Q*(MO) and *Q*(MM′) incorporate characteristics of gas-phase metals in addition to bulk phase enthalpies, making them better at describing interfacial properties and MSIs, the relevance of which has been discussed in earlier works (*10*, *24*). As shown in Fig. 1D, when M changes from early to late TMs on the same oxide, the corresponding *Q*(MO) varies over a range of 12 eV, which is about twice the range of *Q*(MM′) for the same metal on different oxides. However, for late TMs, the corresponding |*Q*(MO)| becomes smaller, particularly for coinage metals, which are <5.1 eV. By contrast, |*Q*(MM′)| of late TMs becomes considerably strong up to 15.6 eV, indicating that MMIs may play a significant role in corresponding MSIs.

Explicit description of MSIs allows us to "recover" all missing E_{adh} in Fig. 1B. As plotted in Fig. 1E, adhesion increase from the weakest of nearly zero at the upper right to the strongest of 309 meV/Å² at the lower left. Systems with weak adhesion typically are less-reactive coinage metals and p-block metals supported on irreducible oxides. Conversely, interfaces exhibiting strong adhesion generally feature early TMs. For late TMs, the corresponding $|E_{adh}|$ depend sensitively on supports, varying from a weak adhesion of 3 meV/Å² to a strong adhesion of 241 meV/Å², which indicates the importance of support effects.

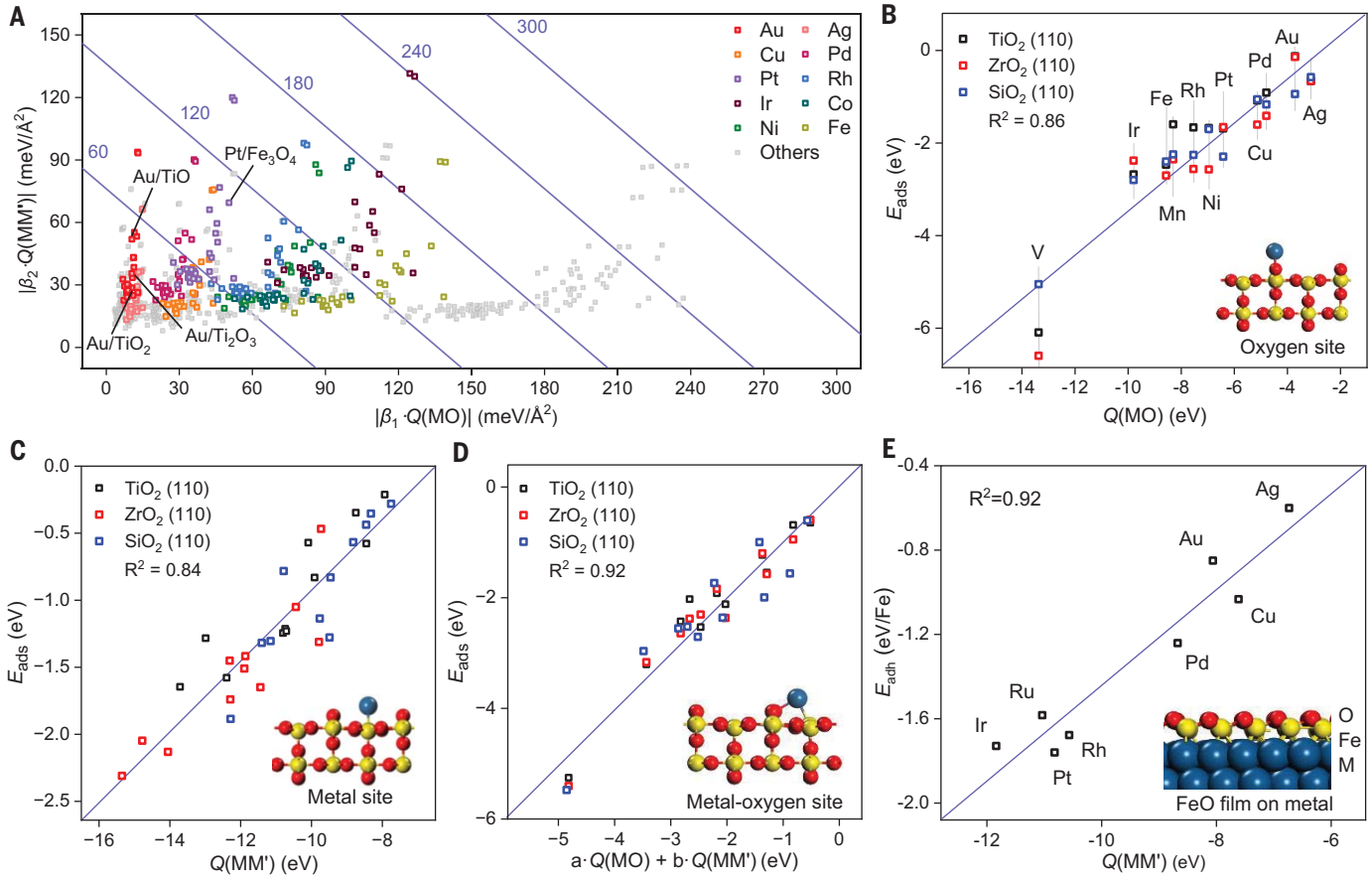

Fig. 2. Nature of the MSIs and applications in different interfacial systems. (**A**) Distribution of metal-oxide systems within the two-dimensional space spanned by $|\beta_2 \cdot Q(MM')|$ and $|\beta_1 \cdot Q(MO)|$ for all considered metal-oxide systems. Contour lines denote increments of $|E_{adh}|$ calculated by the model at the step of 60 meV/Å^2. Selected catalytic systems of interest are highlighted with distinct colors and annotations. (**B**) Correlation between adsorption energy E_{ads} of metal atoms bonding only to oxygen atoms of rutile TiO_2(110), ZrO_2(110), and SiO_2(110) surfaces against Q(MO), with schematic structures shown in insets. The equation for the fitted line is $E_{ads} = 0.47 \cdot Q(MO) + 1.30$ eV. (**C**) E_{ads} of metal atoms bonding only to metal atoms of oxide surfaces against Q(MM') with fitted $E_{ads} = 0.26 \cdot Q(MM') + 1.71$ eV. (**D**) E_{ads} of metal atoms bonding to both metal and oxygen atoms on oxide surfaces against Q(MO) and Q(MM') with fitted $E_{ads} = 0.41 \cdot Q(MO) + 0.03 \cdot Q(MM') + 1.00$ eV. (**E**) Calculated E_{adh} (FeO–M) against Q(MM') for the FeO(111)/M systems with fitted $E_{adh} = 0.23 \cdot Q(MM') + 0.83$ eV/Fe.

The full recovery of E_{adh} makes it possible to predict the contact angle α and thus the stability of all these oxide-supported metal NPs against thermal sintering. Specifically, when MSI is neither too strong nor too weak and has an optimum α of ~90°, the maximum thermal stability could be approached (*11*). Based on the Young–Dupré equation of $|E_{adh}| = \gamma^{M}(1 + \cos\alpha)$, corresponding α of 675 metal-oxide interfaces considered were calculated (Fig. 1F). For group VIII metals on various supports considered, α mainly ranged from 80° to 120°, i.e., near the optimal α. By contrast, coinage metals exhibited weaker MSIs, with most α exceeding 120°, and thus were prone to sintering, which could be mitigated by enhancing MSIs (*31*, *32*).

Nature of MSIs

The above results show that MSIs are determined by the short-range MOI and MMI terms. In fact, under the assumption that MSI is determined by nearest-neighbor bonding across the interface, the formula can be derived analytically, as detailed in the supplementary materials. The derived equation is $E_{adh} = \alpha_1 \cdot Q(MO) + \alpha_2 \cdot Q(MM') + \alpha_0$, where α_1 and α_2 are quantities specifying the number of interfacial metal-oxygen and metal-metal bonds per area units, corresponding to β_1 and β_2 in Eq. 1, and α_0 includes all other uncounted effects. The consistency between the data-driven and derived formulas justifies the physics underlined by MOIs and MMIs, and the data-driven one is versatile in describing realistic metal-oxide interfaces.

Integration of MOIs and MMIs enabled us to disentangle their contributions to the overall MSIs. As plotted in Fig. 2A, the former varies up to ~240 meV/Å^2, twice as large as the range of the latter. In 66% of the 675 metal-oxide combinations, the MOI term was greater than the MMI term. The differences between the two terms could be large, as indicated in fig. S8. For instance, Ni/TiO_2 and Fe/Al_2O_3 have large differences of 45 and 95 meV/Å^2, and corresponding interfaces were primarily composed of metal-oxygen bonds (*33*, *34*). Thus, MOIs dominate the overall strengths of MSIs, which differ greatly from one M to another, manifesting the composition effects of supported metals.

However, the MMI term distinguishes the MSI of a metal catalyst on different metal oxides, manifesting the support effects. To show this, we examined Au NPs on various oxides. Although the MOI term for these systems was small and similar (~10 meV/Å^2), the MMI term was considerable and varied greatly. Specifically, for Au NPs on TiO_2, Ti_2O_3, and TiO sharing the same $|Q(MM')|$, there was a gradual decrease in $|\Delta H_f^{M'O}|$ and thus an increase in β_2, which raises the adhesion energy from 13 to 30 to 49 meV/Å^2. For one metal on oxides with

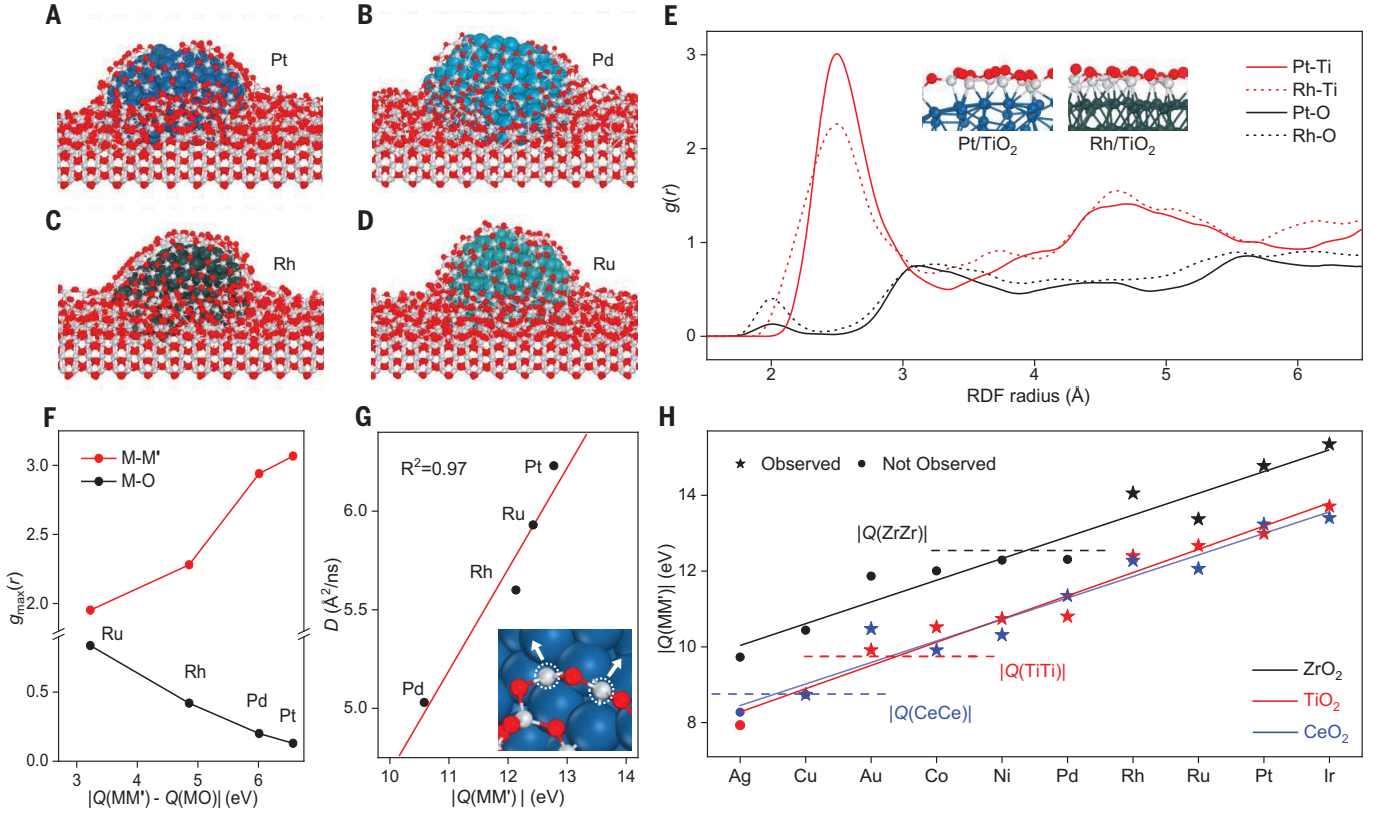

Fig. 3. Strong MMIs and encapsulation occurrence. (**A** to **D**) MD simulations of the encapsulation of the 305-atom Pt, Pd, Rh, and Ru clusters on TiO_2(011) with 12.5% oxygen vacancies at 0.8 ns and 1500 K. Red indicates O atoms and gray Ti atoms; other colors indicate TM atoms. (**E**) RDF of M–M′and M–O bonds at the suboxide-encapsulated and oxide-supported metal interfaces for Pt/TiO_2 and Rh/TiO_2, with insets showing characteristic overlayer structures. (**F**) Intensity of the first peaks of M–M′ and M–O bonds in RDF against |*Q*(MM′) – *Q*(MO)|. (**G**) Diffusion coefficients of M′ atoms for the migration forming the encapsulation overlayers against *Q*(MM′); the inset shows a snap of the migration. (**H**) *Q*(MM′) for late TMs on CeO_2, TiO_2, and ZrO_2 with corresponding M′ affinity of M′ in oxide, *Q*(M′M′) (horizontal dashed lines). Solid lines indicate guiding eyes; stars indicate systems with experimental encapsulation observations (data S5); and circles indicate systems that as yet have no observational evidence.

different oxidant states, the lower the oxidant state, the stronger the MSI strength. For supported metal NPs, particularly coinage metals with weak oxophilic MSIs, this trend implies that exposing metal-rich surfaces or introducing more oxygen vacancies in supports can effectively strengthen MSIs (*35*, *36*). For Pt on different oxides, although the MOI term increased up to 53 meV/Å^2, the MMI term ranged from 30 to 120 meV/Å^2. This comes in addition from substantial enhancement of |*Q*(MM′)| of Pt from 7.5 to 14.8 eV, showing the dominance of M′ affinity of late TM catalysts to MSI.

Unlike particle adhesion, which necessitates features such as those in β_1 and β_2 to capture complex interfacial interactions, adsorptions of metal atoms on oxides could be described directly by *Q*(MO) and *Q*(MM′). We performed DFT calculations for adsorption energies E_{ads} of late TM atoms on rutile TiO_2(110), ZrO_2(110), and SiO_2(110) (see the supplementary materials). When M atoms are adsorbed at O–O bridge sites, bonding exclusively with surface O, E_{ads} is a linear function of *Q*(MO) (Fig. 2B, R^2 = 0.86). Similarly, for those at M′–M′ bridge sites, where only MMI exists, it is a linear function of *Q*(MM′) (Fig. 2C, R^2 = 0.84). When atoms adsorb at O–M′ bridge sites, involving both MOI and MMI, E_{ads} becomes a linear combination of *Q*(MO) and *Q*(MM′) (Fig. 2D, R^2 = 0.92).

The MSI theory can be further extended to metal-supported oxide films, which are often used as model systems for studying SMSIs and encapsulation (*37*). We studied the well-documented FeO(111) bilayer film on close-packed late TMs (*38*) and calculated the E_{adh} between FeO and TMs (see the supplementary materials). The optimized structures based on realistic moiré superstructures by DFT (fig. S10) showed that the Fe layer directly bonds with TM substrates. This configuration suggests that interfacial adhesion is governed by the M–Fe bonding strengths, *Q*(MM′). The calculated E_{adh} should depend linearly on *Q*(MM′) (R^2 = 0.92), as confirmed in Fig. 2E. In other words, the stronger the M′ affinity, the stronger the adhesion. Pt, Rh, Ir, Ru, and Pd exhibited strong adhesion, exceeding 1.24 eV/Fe atom (175 meV/Å^2). In fact, encapsulation was found for those TM NPs supported on iron oxides, but not for other TM NPs (*39*), indicating the crucial role of strong M′ affinity of supported metal M in encapsulation, as further discussed below.

Principle of strong MMIs for encapsulation

The nature of classic SMSI and encapsulation can be explained with the above MSI theory. We used MD simulations to investigate classic SMSI systems of rutile TiO_2(011)–supported 305-atom Pt, Pd, Rh, and Ru clusters (~3 nm in diameter) under elevated temperatures. The optimized α on pristine surfaces ranged from 106° to 122°, indicating that the corresponding MSIs were relatively weak. Cu and Ag were also considered for comparison. To model reduction conditions without including reductants explicitly, 12.5% oxygen vacancies were introduced (see the supplementary materials). For Pt, Pd, Rh, and Ru, with strong M′ affinity [|*Q*(MM′)| > 10.8 eV], migration of TiO_{2-x} suboxide onto the metal NPs was observed during 0.8-ns simulations, and the encapsulation overlayer

formed (Fig. 3, A to D, and movies S1 to S4). Encapsulation was observed for those systems in experiments (*15*, *16*). By contrast, for Cu and Ag, with weak M′ affinity [$|Q(MM')| < 8.8$ eV], such migration did not occur within the simulation time (fig. S12), consistent with the absence of experimental observation of encapsulation.

For supported Pt and Pd NPs, the resulted encapsulation layer in the simulation time was a single Ti-suboxide overlayer, with corresponding Ti:O ratios of 1:1.38 and 1:1.29 (Fig. 3, A and B), consistent with the experiments (*37*, *40*, *41*). Compared with the radial distribution function (RDF) before annealing (fig. S14), the peak intensity of the M–M′ bonds increased substantially and became stronger than that of the M–O bonds (Fig. 3E). These characteristics could be used as the fingerprint of encapsulation occurrence. Furthermore, there were Ti atoms permeating into Pt NP to form Pt–Ti alloys (Fig. 3A), consistent with the Pt–Ti metal signals at the interface observed in experiments, where both the migration of suboxide and alloy formation were observed (*37*). For Rh NPs, the primary bonds between the TiO_{2-x} overlayer and Rh NPs remained Rh–Ti bonds, with no permeation of Ti atoms observed (Fig. 3C). The average coordination number and bond length were 1.98 and 2.54 Å, respectively, which is in excellent agreement with the measured 1.9 and 2.53 Å (*23*). This shorter bond length, compared with the 2.68 Å observed in Rh-Ti intermetallic compounds (*42*), reflects consistently the cationic nature of encapsulated Ti atoms.

The agreements with experiments allowed us to explore structure-function relations from MD simulations. Because the peak intensities of RDF for the M–M′ and M–O bonds reflect their population across the interfaces, we plotted corresponding results in Fig. 3F. The peak intensity of the M–M′ bonds increased with $|Q(MM') - Q(MO)|$, whereas that of the M–O bonds decreased. In other words, the larger the M′ affinity than oxophilicity of supported M, the more populated the M–M′ bonds than the M–O bonds.

The migration of suboxide overlayers on metal NP surfaces was found to be led by M′ atoms, the diffusion coefficients D_e of which can be used to quantify the encapsulation kinetics. As plotted in Fig. 3G, calculated D_e was found to be dependent linearly on M′ affinity. The stronger the M′ affinity, the faster the encapsulation kinetics. For Pt with a larger M′ affinity than that of Pd (13.0 versus 10.8 eV), the corresponding D_e was ~20% larger. Strong M′ affinity would promote the migration from the underlying oxide to supported metal NPs, but might be unfavorable for the diffusion of formed suboxide over metal NPs. These results indicate that the former process is the rate-determine step. Therefore, the M′ affinity of supported M determines not only the M–M′ bond population across the encapsulation interfaces, but also the encapsulation kinetics.

Given the crucial role of MMI in encapsulation, how strong must it be for this process to occur? For Pd and Ni NPs on TiO_2, the corresponding $|Q(MM')|$ of 10.8 and 10.7 eV were strong and encapsulations were indeed observed (*8*, *43*). However, for ZrO_2 support with an ~1.5 eV stronger $|Q(MM')|$ than that of TiO_2 (table S6), no encapsulation was observed. Thus, strong M′ affinity alone is not sufficient. In fact, a stronger Zr affinity of Pd and Ni comes from the more active nature of Zr than Ti, as shown by its larger $|Q(M'M')|$ (12.54 versus 9.76 eV). Thus, for encapsulation to occur, relative strength may be more essential, i.e., requiring M′ affinity of supported M to be stronger than that of M′ in oxide support:

$$|Q(MM')| > |Q(M'M')| \quad (3)$$

Based on the definition of Q, the criterion proposed can be reformulated as $\Delta H_f^{MM'} + \left(\Delta H_{sub}^{M'} - \Delta H_{sub}^{M}\right) < 0$. This implies that both the exothermic mixing M′ in M at infinite dilution and low sublimation enthalpy of M′ with respect to M would facilitate the encapsulation. As a reference, the corresponding $\Delta H_f^{MM'}$ and $\Delta H_{sub}^{M'} - \Delta H_{sub}^{M}$ for porotype systems considered are plotted in fig. S16.

To substantiate the criterion, we examined 10 late TMs on 16 distinct oxide supports with diverse compositions and chemical states, including nearly all experimentally reported encapsulation systems. All of these encapsulations satisfied the proposed criterion. The corresponding M′ affinity of late TMs on tetravalent oxides of ZrO_2, TiO_2, and CeO_2 are plotted in Fig. 3H, along with the M′ affinity of M′ in oxides. For convenience, whether encapsulation was observed experimentally was also indicated. Among considered metals, Ir, Pt, Ru, and Rh exhibited a stronger M′ affinity than that of the oxides considered, resulting in encapsulation exclusively, although more severe conditions are required for ZrO_2 than TiO_2 and CeO_2 (*17*). By contrast, Ag showed a lower M′ affinity than corresponding $|Q(M'M')|$, lacking intrinsic driving force for encapsulation of these oxides.

For Pd, Ni, Co, Au, and Cu, with medium M′ affinity, their relative strengths $|Q(MM')|$ with respect to $|Q(M'M')|$ became sensitive to the oxides. Pd, Ni, Co, and Au exhibited encapsulations on both CeO_2 and TiO_2, whereas this occurred for Cu on CeO_2 (*44*). However, none of these five metals met the criterion for ZrO_2, and no encapsulation was observed. Encapsulation for remaining supports, including Fe_3O_4, ZnO, Al_2O_3, SiO_2, and MgO, are discussed in the supplementary materials. Note that SiO_2 and Al_2O_3, with medium $|Q(M'M')|$ of 9.5 and 6.8 eV, respectively, which were once considered as nonencapsulation supports because of their nonreducibility and weak MSIs, were found to be capable of encapsulation under harsh conditions (*45*) and also satisfy the proposed criterion.

Given the complexity of encapsulation processes and agreement with extensive experimental observations, the criterion of strong MMI in Eq. 3 for suboxide encapsulation of supported metal catalysts is substantiated. In the future, more encapsulation systems could be discovered, such as Ir on more oxides and late TMs on manganese oxide and chromium oxide, as predicted by the theory (data S4). Because the criterion is metal dependent only, it might apply to other metal compound supports. The developed MSI theory therefore offers a constructive guideline to engineer interfaces between metals and supports for the design of more efficient catalysts.

REFERENCES AND NOTES

1. L. Liu, A. Corma, *Chem. Rev.* **118**, 4981–5079 (2018).
2. B. Roldan Cuenya, *Acc. Chem. Res.* **46**, 1682–1691 (2013).
3. C. Vogt, B. M. Weckhuysen, *Nat. Rev. Chem.* **6**, 89–111 (2022).
4. A. J. Medford *et al*., *J. Catal.* **328**, 36–42 (2015).
5. Y. Dai, P. Lu, Z. Cao, C. T. Campbell, Y. Xia, *Chem. Soc. Rev.* **47**, 4314–4331 (2018).
6. B. C. Gates, A. Katz, J. Liu, *Precis. Chem.* **1**, 3–13 (2023).
7. T. W. van Deelen, C. Hernández Mejía, K. P. de Jong, *Nat. Catal.* **2**, 955–970 (2019).
8. M. Monai *et al*., *Science* **380**, 644–651 (2023).
9. K. Zheng *et al*., *Precis. Chem.* **1**, 530–537 (2023).
10. C. T. Campbell, Z. Mao, *ACS Catal.* **7**, 8460–8466 (2017).
11. S. Hu, W.-X. Li, *Science* **374**, 1360–1365 (2021).
12. H. Frey, A. Beck, X. Huang, J. A. van Bokhoven, M. G. Willinger, *Science* **376**, 982–987 (2022).
13. V. Muravev *et al*., *Science* **380**, 1174–1179 (2023).
14. C. T. Campbell, S. C. Parker, D. E. Starr, *Science* **298**, 811–814 (2002).
15. S. Tauster, S. Fung, R. L. Garten, *J. Am. Chem. Soc.* **100**, 170–175 (1978).
16. M. Xu *et al*., *J. Am. Chem. Soc.* **146**, 2290–2307 (2024).
17. T. Pu, W. Zhang, M. Zhu, *Angew. Chem. Int. Ed.* **62**, e202212278 (2023).
18. N. J. O'Connor, A. Jonayat, M. J. Janik, T. P. Senftle, *Nat. Catal.* **1**, 531–539 (2018).
19. K. Tan, M. Dixit, J. Dean, G. Mpourmpakis, *Ind. Eng. Chem. Res.* **58**, 20236–20246 (2019).
20. S. L. Hemmingson, C. T. Campbell, *ACS Nano* **11**, 1196–1203 (2017).
21. F. Didier, J. Jupille, *Surf. Sci.* **314**, 378–384 (1994).
22. J. Li, *J. Mater. Sci. Lett.* **11**, 903–905 (1992).
23. S. Sakellson, M. McMillan, G. L. Haller, *J. Phys. Chem.* **90**, 1733–1736 (1986).
24. C.-Y. Liu, T. P. Senftle, *Curr. Opin. Chem. Eng.* **37**, 100832 (2022).
25. J. A. Esterhuizen, B. R. Goldsmith, S. Linic, *Nat. Catal.* **5**, 175–184 (2022).
26. W. Shu *et al*., *J. Am. Chem. Soc.* **146**, 8737–8745 (2024).
27. R. Ouyang, S. Curtarolo, E. Ahmetcik, M. Scheffler, L. M. Ghiringhelli, *Phys. Rev. Mater.* **2**, 083802 (2018).
28. S. D. Huang, C. Shang, P. L. Kang, X. J. Zhang, Z. P. Liu, *Wiley Interdiscip. Rev. Comput. Mol. Sci.* **9**, e1415 (2019).
29. C. T. Campbell, J. R. Sellers, *Faraday Discuss.* **162**, 9–30 (2013).
30. A. Miedema, F. De Boer, R. Boom, *Calphad* **1**, 341–359 (1977).
31. J. Zhang *et al*., *J. Am. Chem. Soc.* **144**, 2255–2263 (2022).
32. W. Cai *et al*., *RSC Adv.* **13**, 9010–9019 (2023).
33. M. Xu *et al*., *J. Am. Chem. Soc.* **140**, 11241–11251 (2018).
34. Y. Wang *et al*., *AIP Adv.* **9**, 125313 (2019).
35. Y. Wang *et al*., *J. Catal.* **354**, 46–60 (2017).
36. A. Ruiz Puigdollers, P. Schlexer, S. Tosoni, G. Pacchioni, *ACS Catal.* **7**, 6493–6513 (2017).
37. A. Beck *et al*., *Nat. Commun.* **11**, 3220 (2020).
38. Q. Fu *et al*., *Science* **328**, 1141–1144 (2010).
39. P. Wu *et al*., *Nat. Commun.* **11**, 3042 (2020).

40. F. Pesty, H.-P. Steinrück, T. E. Madey, *Surf. Sci.* **339**, 83–95 (1995).
41. S. Zhang *et al*., *Nano Lett.* **16**, 4528–4534 (2016).
42. D. Koningsberger, J. Martens, R. Prins, D. Short, D. Sayers, *J. Phys. Chem.* **90**, 3047–3050 (1986).
43. J. Sá, J. Bernardi, J. A. Anderson, *Catal. Lett.* **114**, 91–95 (2007).
44. X. Wang *et al*., *ACS Appl. Energy Mater.* **1**, 1408–1414 (2018).
45. F. Yang *et al*., *Chem. Sci.* **12**, 12651–12660 (2021).
46. T. Wang *et al*., Zenodo (2024); https://doi.org/10.5281/zenodo.13854584.

ACKNOWLEDGMENTS

We thank C. T. Campbell for comments. **Funding:** This work was supported by the National Natural Science Foundation of China (grants 22221003, 22432004, 22173058, 22372153, and 91945302), the Innovation Program for Quantum Science and Technology (grant 2021ZD0303302), the Strategic Priority Research Program of the Chinese Academy of Sciences (grant XDB0450102), the National Key Research and Development Program of China (grant 2021YFB3502000), the National Program for Support of Top-notch Young Professional Fundamental Research Funds for the Central Universities (grant 20720220009), and the Supercomputer Center of University of Science and Technology of China and the Hefei Advanced Computing Center. **Author contributions:** W.L. conceived and supervised the project. T.W. and R.O. performed machine learning. T.W. and Y.W. performed density functional theory calculations. J.H. and T.W. performed molecular dynamics simulations and encapsulation. W.L., T.W., R.O., J.H., S.H., and Y.H. analyzed and discussed the results. W.L., T.W., R.O., S.H., and J.H. wrote the paper. **Competing interests:** The authors declare that no competing interests. **Data and materials availability:** All data needed to evaluate the conclusions are present in the main text or the supplementary materials, including data S1 to S6 and movies S1 to S4, or have been deposited at Zenodo (*46*).

SUPPLEMENTARY MATERIALS

Submitted 30 July 2024; accepted 22 October 2024
10.1126/science.adp6034